

Research Article

Discontinuous Deformation Analysis Based on Wachspress Interpolation Function for Detailed Stress Distribution

W. Jiang ^{1,2}, Y. H. Wang,¹ G. H. Sun,² P. C. Song,¹ and C. Mao¹

¹Hubei Key Laboratory of Disaster Prevention and Mitigation, China Three Gorges University, Yichang, Hubei 443002, China

²State Key Laboratory of Geomechanics and Geotechnical Engineering, Institute of Rock and Soil Mechanics, Chinese Academy of Sciences, Wuhan 430071, China

Correspondence should be addressed to W. Jiang; jiangweilion@163.com

Received 5 April 2018; Accepted 1 June 2018; Published 26 June 2018

Academic Editor: Petr Krysl

Copyright © 2018 W. Jiang et al. This is an open access article distributed under the Creative Commons Attribution License, which permits unrestricted use, distribution, and reproduction in any medium, provided the original work is properly cited.

In the original discontinuous deformation analysis (DDA) method, the complete first-order displacement function is used to describe block movement and deformation, which induce constant stress and strain throughout the block. To achieve a more detailed stress distribution, Wachspress interpolation displacement function is employed to express the displacement of blocks in DDA, and the interactions between blocks are still governed under the original DDA. Displacements of the vertices of all blocks constitute new freedom vectors, and the stiffness and force matrix formulations are derived again. In the new formulation, Wachspress interpolation ensures that the edges of the blocks are straight; therefore, contact detection can be processed based on the original DDA. Several classical examples are analyzed. The results show that the new formulation obtains similar configurations as the original DDA but provides more detailed and continuous stress distributions within block element.

1. Introduction

The discontinuous deformation analysis (DDA) method, which was proposed by Shi [1] in 1988, represents a novel method of analyzing the dynamic mechanical behavior of block systems under large displacement. As a theoretically rigorous numerical method, the DDA has been a focus of the discontinuous computing field since it was first proposed, and it has been used to address diverse problems in geotechnical engineering, such as landslide simulations [2], rock slope stability assessments [3], rockfall path tracking [4], blasting effect evaluation [5], stability analysis of tunnels [6], analysis of the shear creep deformation of structural planes [7], simulation of the fracturing process initiated by hydraulic pressure [8], crack propagation modeling [9], and seismic wave propagation modeling [10].

After numerous enhancements, the DDA has matured to solve more complicated problems. Solutions have been proposed to restrain false volume expansion when simulating large rotation, such as adopting the second-order approximation of $\sin \theta$ and $\cos \theta$ in the shape function [11], executing a postadjustment once the open-close iteration

converges [12], introducing a new displacement variable based on the trigonometric function transformations [13] and accumulating the total strain components in fixed local frames [14]. To avoid the introduction of virtual springs, which are commonly used in classical DDA, the DDA has been successfully reconfigured using the Lagrange multiplier method [15], the complementarity theory [16], and the variational inequality theory [17]. Recently, a dual-form DDA has been proposed by Zheng [18], in which the contact forces instead of the block displacements are utilized as the basic variables and the compatibility iteration for the quasi-variational inequality guarantees the convergence and solution efficiency. To improve the efficiency of disk-based DDA, Beyabanaki and Bagtzoglou [19] presented a new contact model for nonrigid disks, in which disk-disk and disk-boundary contacts are transformed into point-to-line contacts. To simulate progressive failure, Jiang et al. [20] introduced a viscous damping component to absorb the kinetic energy of discrete blocks and defined convergence criteria for DDA solutions, which provided more objective standards for the application of the DDA.

Considering that 3D analyses are always preferred for practical engineering problems, many researchers are working on expanding the original 2D DDA to a 3D version. When the blocks have been identified via 3D discontinuities cutting [21], detecting contact rapidly and reliably appears to be the major barrier to developing an efficient 3D DDA. Contact algorithms, such as the incision body method [22], fast common plane method [23], and main plane method [24], have already been suggested. Recently, Shi [25] suggested a new contact theory named the $E(A,B)$ algorithm, and it provides a more robust method of eliminating the greatest obstacle in 3D DDA programming.

In the original DDA, the first-order displacement function is adopted to describe the block movement and deformation, which induce constant stress and strain throughout the block. More exact stress distribution within block element is beneficial to the analysis of practical problems, and several approaches for determining such distributions have been attempted. One method is to assemble small blocks to form a larger block by adopting artificial joints and subblocks [26, 27]. When the subblocking method is used, the constraints between subblocks must be accurately imposed for reasonably reflecting the deformation of an actual block, which is difficult in practical applications. Another approach is to use high-order displacement functions in the DDA [1]. The second-order and third-order displacement functions have been successfully implemented [28, 29], and the ability to model complicated stress and strain fields have been verified. If high-order displacement functions are used, then the edges of a block are likely to be transformed to curves. Thus, the dissection of edges should be executed to exactly impose contact conditions, which is an additional troublesome job. In addition, scholars have added finite element meshes in blocks so that stress variations within the blocks can be evaluated [30, 31]. Considering that the finite element method (FEM) is familiar to researchers, this process is well understood. However, when the deformation and displacement of one block are illustrated by inner finite elements [32], the stress and strain fields are usually discontinuous within the block, which appears to represent a drawback compared with the adoption of high-order displacement functions in the DDA. To some degree, these attempts have successfully acquired more complicated stress and strain fields than the original DDA; however, extra tasks are likely involved or advantages of the original DDA may be lost.

Over the past two decades, the polygonal finite element method (PFEM) has achieved remarkable progress in theory and application [33, 34], and it provides new techniques for attaining a more detailed stress distribution of blocks in DDA. Some interpolations, e.g., Wachspress interpolation [35], Laplace interpolation [36], Sibson interpolation [37], and Maximum entropy interpolation [38], were proposed for constructing displacement functions in the PFEM. All displacement functions based on these interpolations have the ability to produce straight edges on polygons undergoing deformation. To begin with, Wachspress interpolation that originated from projective geometry defines the shape function at point \mathbf{x} using areas of triangular composed of point \mathbf{x} and the vertices. The gradient of the shape function

can be derived directly, which facilitates the calculation of strain and stiffness matrices for elastic analysis. Because the shape function is defined in the Cartesian coordinate system, the numerical integration could be performed on the physical elements. Then, both Sibson and Laplace interpolation are natural neighbor-based interpolations, which define the shape function at point \mathbf{x} using the information of Voronoi cells or Voronoi edges. For a better implementation, the isoparametric mapping and reference elements are usually involved in the computation [39]. Furthermore, enlightened by the Shannon entropy problem [40] in information theory, maximum entropy interpolation proposed by Sukumar [38] derives the shape function at point \mathbf{x} from a constrained optimization problem. Calculating the shape function requires solving an optimization problem by numerical iteration, which means that the subsequent computation is more complicated. By comparison, DDA users will have an easier access to Wachspress interpolation for little prior knowledge is involved, and Wachspress interpolation has a better performance being enrolled in the DDA codes. Therefore, Wachspress interpolation function is adopted in this paper to govern the displacement of each block in DDA. After contact detection in Cartesian coordinate system, the contact constraints between blocks are enforced as the original DDA. The displacements of vertexes of blocks constitute new freedom vectors and formulations for the modified DDA are derived. The C++ computer codes are developed for the new formulation and are used to solve several examples. The ability of the proposed scheme to obtain more detailed stress distributions within block elements is well verified by the calculated results.

2. Displacement Function of Blocks Based on Wachspress Interpolation

In the DDA method, the deformations and large displacements represent the accumulation of incremental displacements and deformations over many time steps. The movement and deformation of the I th block within one time step are originally defined by six independent variables as follows:

$$\mathbf{d}_I = (u_0 \ v_0 \ r_0 \ \varepsilon_x \ \varepsilon_y \ \gamma_{xy})^T \quad (1)$$

where u_0 and v_0 are the incremental displacement components of the centroid point (x_o, y_o) of the I th block in the horizontal and vertical directions, respectively; r_0 is the incremental rigid rotation angle around point (x_o, y_o) ; and $(\varepsilon_x, \varepsilon_y, \gamma_{xy})$ represents the incremental strains based on a small deformation assumption. The incremental displacement \mathbf{u} at any point (x, y) in the I th block can be related to \mathbf{d}_I :

$$\mathbf{u} = (u \ v)^T = \mathbf{T}_I \mathbf{d}_I \quad (2)$$

where \mathbf{T}_I is called the displacement transformation matrix of the block.

$$\mathbf{T}_I = \begin{bmatrix} 1 & 0 & -(y - y_o) & (x - x_o) & 0 & (y - y_o)/2 \\ 0 & 1 & (x - x_o) & 0 & -(y - y_o) & (x - x_o)/2 \end{bmatrix} \quad (3)$$

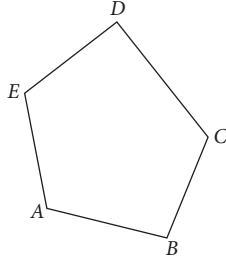


FIGURE 1: Pentagon defined by the Wachspress interpolation.

Expression (2) has been verified to be the complete first-order displacement function [1]; therefore, each block presents constant stress and strain, which creates an obstacle to acquiring a more detailed stress distribution. Because most of the blocks in the DDA are polygons, Wachspress interpolation has great potential to be used developing a new displacement function for blocks. When Wachspress interpolation is employed to express the displacement of one block, the incremental displacements u and v of the vertexes form a new freedom vector of the block. Assuming that the I th block contains n vertexes within the current time step, \mathbf{d}_I could be rewritten as follows:

$$\mathbf{d}_I = (u_1 \ v_1 \ u_2 \ v_2 \ \cdots \ u_n \ v_n)^T \quad (4)$$

where u_j and v_j are the incremental displacement components of the j th vertex in the horizontal and vertical directions.

Wachspress interpolation requires that the shape function satisfies certain basic principles. For example, the five vertexes of a pentagon are arranged counterclockwise (shown in Figure 1). For the vertex A , the edges including A are called adjacent edges of A , such as AB and EA , and the other edges are called opposite edges of A , such as BC , CD , and DE .

The shape function $N_i(\mathbf{x})$ must satisfy the following criteria:

- (1) Continuous within the whole polygon;
- (2) A δ function at vertexes, i.e.,

$$N_i(\mathbf{x}_j) = \delta_{ij} \quad (5)$$

- (3) Linear on adjacent edges
- (4) Zero on opposite edges

Wachspress pointed out that a rational function could be adopted to build the required shape function and proposed an algebraic geometry approach to accomplishing this task [35]. Because the algebraic geometry approach is complex and impractical when the polygon has a large number of edges, some enhancements have been made to perfect the construction method of a shape function. The construction scheme proposed by Malsch and Dasgupta [39] is acknowledged as the simplest and most practical. Malsch and Dasgupta proposed that the shape function could be written as follows:

$$N_i(x, y) = \frac{A(P_{i-1}, P_i, P_{i+1}) (\prod_{k \neq i, i-1} A(P, P_k, P_{k+1}))}{\sum_{j=1}^n A(P_{j-1}, P_j, P_{j+1}) (\prod_{k \neq j, j-1} A(P, P_k, P_{k+1}))} \quad (6)$$

where P_1, P_2, \dots, P_n are the vertexes of a polygon arranged counterclockwise, $P(x, y)$ is any point within the polygonal element, and $A(\cdot, \cdot, \cdot)$ is the area of a triangle determined by three points. An analysis of (6) indicates that the four basic principles are completely satisfied.

The incremental displacement at any point (x, y) in the block can be expressed as follows:

$$\mathbf{u} = \begin{pmatrix} u \\ v \end{pmatrix} = \begin{pmatrix} N_1 & 0 & N_2 & 0 & \cdots & \cdots & N_n & 0 \\ 0 & N_1 & 0 & N_2 & \cdots & \cdots & 0 & N_n \end{pmatrix} \mathbf{d}_I \quad (7)$$

$$= \mathbf{N}_I \mathbf{d}_I$$

where N_j is the shape function (6) associated with the j th vertex. For a point (x, y) on the boundary of a block, its displacement \mathbf{u} is actually a linear interpolation between the displacements of two relevant vertexes [35]. Adopting the displacement function (7), the edges of a block will still be straight lines after deformation, which is beneficial to contact detection.

Obviously, the shape function (6) can be replaced by a simpler formulation in the case of limited vertexes, such as a triangular finite element ($n=3$) or a quadratic finite element ($n=4$) with shape functions familiar to scholars. In this study, the shape function (6) is employed regardless of the number of vertexes because it has been verified that the element with shape function (6) will degenerate to those two classical finite elements if $n=3$ or $n=4$, which is beneficial to uniformly program codes.

Once the incremental displacement \mathbf{d}_I is obtained through the open-close iteration, the incremental strain vector $\boldsymbol{\varepsilon}$ within the current time step can be calculated as follows:

$$\boldsymbol{\varepsilon} = \begin{pmatrix} \varepsilon_x \\ \varepsilon_y \\ \gamma_{xy} \end{pmatrix} = \begin{pmatrix} \frac{\partial N_1}{\partial x} & 0 & \frac{\partial N_2}{\partial x} & 0 & \cdots & \cdots & \frac{\partial N_n}{\partial x} & 0 \\ 0 & \frac{\partial N_1}{\partial y} & 0 & \frac{\partial N_2}{\partial y} & \cdots & \cdots & 0 & \frac{\partial N_n}{\partial y} \\ \frac{\partial N_1}{\partial y} & \frac{\partial N_1}{\partial x} & \frac{\partial N_2}{\partial y} & \frac{\partial N_2}{\partial x} & \cdots & \cdots & \frac{\partial N_n}{\partial y} & \frac{\partial N_n}{\partial x} \end{pmatrix} \mathbf{d}_I \quad (8)$$

$$= \mathbf{B}_I \mathbf{d}_I$$

in which \mathbf{B}_I is the strain matrix similar to the FEM and represents the relationship between strain and freedom. The incremental stress vector $\boldsymbol{\sigma}$ of the block is calculated by

$$\boldsymbol{\sigma} = \mathbf{D}_I \boldsymbol{\varepsilon} \quad (9)$$

in which

$$\boldsymbol{\sigma} = (\sigma_x \ \sigma_y \ \tau_{xy})^T \quad (10)$$

and \mathbf{D}_I is the elastic matrix of the I th block. In the case of plane strain, \mathbf{D}_I is

$$\mathbf{D}_I = \frac{E_I(1-\nu_I)}{(1+\nu_I)(1-2\nu_I)} \begin{bmatrix} 1 & \frac{\nu_I}{1-\nu_I} & 0 \\ \frac{\nu_I}{1-\nu_I} & 1 & 0 \\ 0 & 0 & \frac{1-2\nu_I}{2(1-\nu_I)} \end{bmatrix} \quad (11)$$

where E_I is Young's modulus and ν_I is Poisson's ratio.

The total stress vector is accumulated as

$$\boldsymbol{\sigma}^m = \boldsymbol{\sigma}^{m-1} + \boldsymbol{\sigma} \quad (12)$$

where $\boldsymbol{\sigma}^m$ represents the total stress vector of the block at the end of the m th time step and will be treated as the initial stress for the next time step.

3. Equilibrium Equations of the Block System

Because the DDA method applies the minimum total potential energy principle, for each block, the total potential energy is the summation of all potential energy sources, which include the elastic deformation of the block, initial stresses, point loads on the block, volume forces, and inertial forces. If one block contacts other adjacent blocks, the potential energy induced by contact forces or friction forces contributes to the total potential energy of the block.

Fixed points are abandoned in the new procedure. In the original DDA, fixed points are employed to enforce the displacement boundary conditions, and the potential energy induced by those constraint displacement points must be added to the total potential energy. However, because the new procedure considers the displacement of block vertexes as freedom vectors, displacement boundary conditions can be compulsively enforced by modifying the ultimate global stiffness matrix and load vector similar to the FEM; therefore, the potential energy associated with displacement boundary conditions is excluded from the total potential energy.

For a block system with N blocks, to minimize the total potential energy, the equilibrium equations within the current time step can be expressed in the following matrix form:

$$\begin{bmatrix} \mathbf{K}_{11} & \mathbf{K}_{12} & \mathbf{K}_{13} & \cdots & \mathbf{K}_{1N} \\ \mathbf{K}_{21} & \mathbf{K}_{22} & \mathbf{K}_{23} & \cdots & \mathbf{K}_{2N} \\ \mathbf{K}_{31} & \mathbf{K}_{32} & \mathbf{K}_{33} & \cdots & \mathbf{K}_{3N} \\ \vdots & \vdots & \vdots & \ddots & \vdots \\ \mathbf{K}_{N1} & \mathbf{K}_{N2} & \mathbf{K}_{N3} & \cdots & \mathbf{K}_{NN} \end{bmatrix} \begin{bmatrix} \mathbf{d}_1 \\ \mathbf{d}_2 \\ \mathbf{d}_3 \\ \vdots \\ \mathbf{d}_N \end{bmatrix} = \begin{bmatrix} \mathbf{F}_1 \\ \mathbf{F}_2 \\ \mathbf{F}_3 \\ \vdots \\ \mathbf{F}_N \end{bmatrix} \quad (13)$$

where \mathbf{d}_I is the displacement variables of block I and \mathbf{F}_I is the generalized load vector acting on block I , and these variables are represented by $2n_I \times 1$ matrices (n_I represents the number of vertexes on block I). The stiffness matrix \mathbf{K}_{II} is a $2n_I \times 2n_I$ matrix depending on the material properties of block I , and $\mathbf{K}_{IJ(I \neq J)}$ is a $2n_I \times 2n_J$ matrix defined by the contacts between block I and J .

In this section, based on the minimum total potential energy principle, the submatrices induced by all potential energy sources except the contact constraints are derived.

3.1. Submatrix of Block Elastic Deformation. The strain energy \prod_e of the elastic stresses of the I th block is derived as follows:

$$\prod_e = \iint \frac{1}{2} (\varepsilon_x \sigma_x + \varepsilon_y \sigma_y + \gamma_{xy} \tau_{xy}) dx dy \quad (14)$$

In (14), the integration is performed over the entire area of the I th block. For each time step, the blocks are assumed to be linearly elastic; therefore, the relationship between stress and strain can be denoted as follows:

$$\boldsymbol{\sigma}_I = \mathbf{D}_I \boldsymbol{\varepsilon}_I \quad (15)$$

Therefore, the strain energy of (14) can be expressed as follows:

$$\begin{aligned} \prod_e &= \iint \frac{1}{2} \boldsymbol{\varepsilon}_I^T \mathbf{D}_I \boldsymbol{\varepsilon}_I dx dy \\ &= \frac{1}{2} (\mathbf{d}_I)^T \iint (\mathbf{B}_I)^T \mathbf{D}_I (\mathbf{B}_I) dx dy (\mathbf{d}_I) \end{aligned} \quad (16)$$

If the strain energy is minimized by derivation, the stiffness matrix of the I th block will be obtained and can then be added to the global stiffness matrix:

$$\iint (\mathbf{B}_I)^T \mathbf{D}_I (\mathbf{B}_I) dx dy \rightarrow \mathbf{K}_{II} \quad (17)$$

3.2. Submatrix of Initial Stress. The accumulated stresses over the previous time steps will be transferred to the next step as the initial stress loading, which means that the stress $\boldsymbol{\sigma}^m$ in (12) will be considered the initial stress for time step $m+1$. The potential energy of the initial stress is given as follows:

$$\begin{aligned} \prod_{\sigma^m} &= \iint (\varepsilon_x \sigma_x^m + \varepsilon_y \sigma_y^m + \gamma_{xy} \tau_{xy}^m) dx dy \\ &= \iint (\boldsymbol{\varepsilon}_I)^T (\boldsymbol{\sigma}^m) dx dy \\ &= (\mathbf{d}_I)^T \iint (\mathbf{B}_I)^T (\boldsymbol{\sigma}^m) dx dy \end{aligned} \quad (18)$$

If \prod_{σ^m} is minimized by derivation, the following $2n_I \times 1$ vector will be obtained and can then be added to the vector \mathbf{F}_I in the global force vector:

$$- \iint (\mathbf{B}_I)^T (\boldsymbol{\sigma}^m) dx dy \rightarrow \mathbf{F}_I \quad (19)$$

3.3. Submatrix of Point Loading. Assuming that the point loading force (F_x, F_y) acts on any point (x_0, y_0) within the I th block, the potential energy of this point loading is as follows:

$$\begin{aligned} \prod_p &= - (F_x u + F_y v) = - (u \ v) \begin{pmatrix} F_x \\ F_y \end{pmatrix} \\ &= - (\mathbf{d}_I)^T \mathbf{N}_I (x_0, y_0)^T \begin{pmatrix} F_x \\ F_y \end{pmatrix} \end{aligned} \quad (20)$$

If \prod_p is minimized by derivation, then the following $2n_I \times 1$ vector will be obtained and can be added to the vector \mathbf{F}_I in the global force vector:

$$\mathbf{N}_I(x_0, y_0)^T \begin{pmatrix} F_x \\ F_y \end{pmatrix} \rightarrow \mathbf{F}_I \quad (21)$$

3.4. Submatrix of Volume Forces. Assuming that (b_x, b_y) represents the constant body forces acting on the entire volume of the I th block, the potential energy induced by body forces is as follows:

$$\begin{aligned} \prod_b &= - \iint (b_x u + b_y v) dx dy \\ &= - \iint (u \ v) \begin{pmatrix} b_x \\ b_y \end{pmatrix} dx dy \\ &= - (\mathbf{d}_I)^T \iint (\mathbf{N}_I)^T dx dy \begin{pmatrix} b_x \\ b_y \end{pmatrix} \end{aligned} \quad (22)$$

If \prod_b is minimized by derivation, the following $2n_I \times 1$ vector will be obtained and can be added to the vector \mathbf{F}_I in the global force vector:

$$\iint (\mathbf{N}_I)^T dx dy \begin{pmatrix} b_x \\ b_y \end{pmatrix} \rightarrow \mathbf{F}_I \quad (23)$$

3.5. Submatrix of Inertial Forces. In the DDA, the time steps are used in both static and dynamic analyses. The static analysis assumes that the initial velocity at the beginning of the current time step is 0. When the dynamic analysis is executed, the velocity at the end of the previous time step is used as the initial velocity at the beginning of the current time step. The term $(u(t), v(t))$ denotes the time-dependent displacement of any point (x, y) of the I th block and M denotes the mass per unit area; thus, the inertial force acting on a per unit area is as follows:

$$\begin{pmatrix} f_x \\ f_y \end{pmatrix} = -M \frac{\partial^2}{\partial t^2} \begin{pmatrix} u(t) \\ v(t) \end{pmatrix} = -M \mathbf{N}_I \frac{\partial^2 \mathbf{d}_I(t)}{\partial t^2} \quad (24)$$

The potential energy of the inertial force is given as follows:

$$\begin{aligned} \prod_i &= - \iint (u \ v) \begin{pmatrix} f_x \\ f_y \end{pmatrix} dx dy \\ &= \iint M (\mathbf{d}_I)^T (\mathbf{N}_I)^T (\mathbf{N}_I) \frac{\partial^2 \mathbf{d}_I(t)}{\partial t^2} dx dy \end{aligned} \quad (25)$$

The Newmark scheme is adopted to dispose the accelerated velocity as the original DDA. We have

$$\frac{2M}{\Delta^2} \iint (\mathbf{N}_I)^T (\mathbf{N}_I) dx dy \rightarrow \mathbf{K}_{II} \quad (26)$$

and

$$\frac{2M}{\Delta} \iint (\mathbf{N}_I)^T (\mathbf{N}_I) dx dy (\mathbf{V}_{0I}) \rightarrow \mathbf{F}_I \quad (27)$$

where Δ is the time interval of the present time step and \mathbf{V}_{0I} is the velocity at the end of the previous time step.

3.6. Numerical Integration Scheme. Collecting the contributions of all potential energy sources mentioned above, we have

$$\begin{aligned} \mathbf{K}_{II} &= \iint (\mathbf{B}_I)^T \mathbf{D}_I (\mathbf{B}_I) dx dy \\ &+ \frac{2M}{\Delta^2} \iint (\mathbf{N}_I)^T (\mathbf{N}_I) dx dy \\ \mathbf{F}_I &= - \iint (\mathbf{B}_I)^T (\boldsymbol{\sigma}^m) dx dy + \mathbf{N}_I(x_0, y_0)^T \begin{pmatrix} F_x \\ F_y \end{pmatrix} \\ &+ \iint (\mathbf{N}_I)^T dx dy \begin{pmatrix} b_x \\ b_y \end{pmatrix} \\ &+ \frac{2M}{\Delta} \iint (\mathbf{N}_I)^T (\mathbf{N}_I) dx dy (\mathbf{V}_{0I}) \end{aligned} \quad (28)$$

In (28) and (29), the components \mathbf{N}_I and \mathbf{B}_I are actually rational functions, which means that the integration cannot be accomplished analytically. To overcome this problem, the original polygonal block is decomposed to several triangles, and a Hammer integration scheme is employed. The details of the integration scheme are given as follows.

As shown in Figure 2(a), for any given polygon, the integration on the whole area can be obtained as follows:

$$\iint f(x, y) dx dy = \sum_{i=1}^n \iint_{\Delta_i} f(x, y) dx dy \quad (30)$$

For simplicity, each subtriangle is formed by two adjacent vertexes and the centroid point of the original polygon. The Hammer integration provides a simple method of calculating the integration of each subtriangle. According to the Hammer integration,

$$\begin{aligned} \int_{\Delta} f(x, y) dx dy &= \int_{\Delta} f(L_1, L_2, L_3) dx dy \\ &= \sum_{i=1}^m W_i f_i(L_1, L_2, L_3) \end{aligned} \quad (31)$$

where $L_1, L_2,$ and L_3 are the area coordinates of an integration point (x, y) in the triangle and m is the number of integration points within one triangle. If $m=4$, the numerical integration precision of the Hammer integration will reach $O(h^4)$. Four integration points are employed as in Figure 2(b), and their area coordinates and related weighting coefficients are listed as follows:

$$\begin{aligned} \text{Hammer point 1: } L_1 &= 0.33333, L_2 = 0.33333, L_3 \\ &= 0.33333, W = -0.56250000S \end{aligned}$$

$$\begin{aligned} \text{Hammer point 2: } L_1 &= 0.60000, L_2 = 0.20000, L_3 \\ &= 0.20000, W = 0.52083333S \end{aligned}$$

$$\begin{aligned} \text{Hammer point 3: } L_1 &= 0.20000, L_2 = 0.60000, L_3 \\ &= 0.20000, W = 0.52083333S \end{aligned}$$

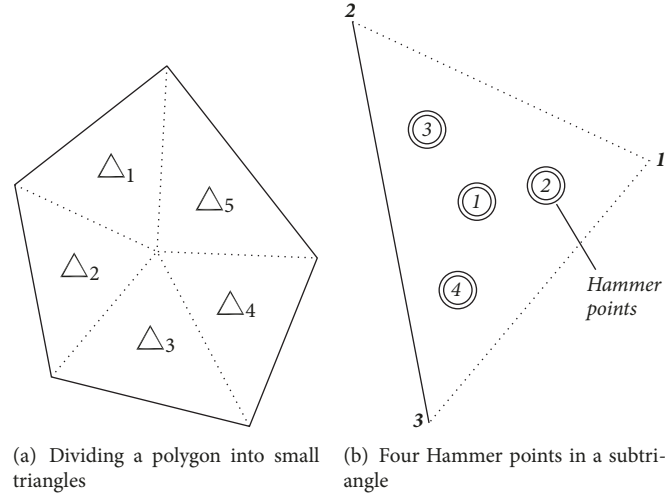


FIGURE 2: Numerical integration scheme.

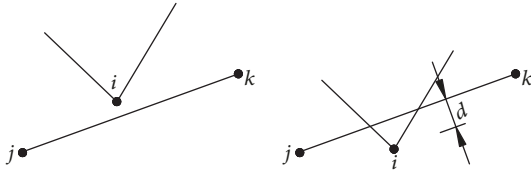


FIGURE 3: Normal spring and its contribution to the global equation.

$$\begin{aligned} \text{Hammer point 4: } L_1 &= 0.20000, L_2 = 0.20000, L_3 \\ &= 0.60000, W = 0.520833333S \end{aligned} \quad (32)$$

where S represents the area of the triangle.

4. Submatrices of the Contacts between Blocks

The advantage of the DDA is the rigorous contact model that governs the interactions of blocks, and the model includes two main steps: “contact detection” and “contact mechanics”. When the displacements of blocks are governed by (7), the edges of blocks remain straight from beginning to end; hence, “contact detection” can be processed as the original DDA. However, because the freedom vectors have been changed in the new formulation, the “contact mechanics” should be adjusted accordingly.

No interpenetration and no tension are required on the contact surface when two adjacent blocks contact. To achieve the contact conditions, stiff springs are applied along normal and tangential directions. In this section, the submatrices related to contact are derived again.

4.1. Normal Stiffness Submatrix. As shown in Figure 3, a vertex i and an entrance line jk constitute a classical contact pair in DDA. The coordinates of point i , j , and k are denoted as (x_i, y_i) , (x_j, y_j) , and (x_k, y_k) , respectively, and the displacements are (u_i, v_i) , (u_j, v_j) , and (u_k, v_k) in the current

time step, respectively. Considering that displacements in each time step are required to be a small value, the first-order infinitesimal value is retained and the second-order infinitesimal value is neglected. The distance d from vertex i to entrance line jk can be expressed as follows:

$$\begin{aligned} d &\approx \frac{\begin{vmatrix} 1 & x_i & y_i \\ 1 & x_j & y_j \\ 1 & x_k & y_k \end{vmatrix} + \begin{vmatrix} 1 & u_i & y_i \\ 1 & u_j & y_j \\ 1 & u_k & y_k \end{vmatrix} + \begin{vmatrix} 1 & x_i & v_i \\ 1 & x_j & v_j \\ 1 & x_k & v_k \end{vmatrix}}{\sqrt{(x_j - x_k)^2 + (y_j - y_k)^2}} \\ &= \frac{S_0}{l} + \frac{1}{l} (y_j - y_k \ x_k - x_j) \begin{pmatrix} u_i \\ v_i \end{pmatrix} \\ &\quad + \frac{1}{l} (y_k - y_i \ x_i - x_k) \begin{pmatrix} u_j \\ v_j \end{pmatrix} \\ &\quad + \frac{1}{l} (y_i - y_j \ x_j - x_i) \begin{pmatrix} u_k \\ v_k \end{pmatrix} \end{aligned} \quad (33)$$

where

$$S_0 = \begin{vmatrix} 1 & x_i & y_i \\ 1 & x_j & y_j \\ 1 & x_k & y_k \end{vmatrix} \quad (34)$$

and

$$l = \sqrt{(x_j - x_k)^2 + (y_j - y_k)^2} \quad (35)$$

Furthermore, d is expressed as a formulation about (u_i, v_i) , (u_j, v_j) , and (u_k, v_k) :

$$\begin{aligned} d &= \frac{S_0}{l} + (e_i \ g_i) \begin{bmatrix} u_i \\ v_i \end{bmatrix} + (e_j \ g_j) \begin{bmatrix} u_j \\ v_j \end{bmatrix} \\ &\quad + (e_k \ g_k) \begin{bmatrix} u_k \\ v_k \end{bmatrix} \end{aligned} \quad (36)$$

in which

$$\begin{aligned}
 e_i &= \frac{y_j - y_k}{l}, \\
 g_i &= \frac{x_k - x_j}{l}, \\
 e_j &= \frac{y_k - y_i}{l}, \\
 g_j &= \frac{x_i - x_k}{l}, \\
 e_k &= \frac{y_i - y_j}{l}, \\
 g_k &= \frac{x_j - x_i}{l}.
 \end{aligned} \tag{37}$$

To satisfy the no interpenetration requirement, the normal spring is added when $d < 0$, and the deformation energy of the normal spring is as follows:

$$\Pi_k = \frac{p}{2} d^2 \tag{38}$$

where p is the stiffness of the normal spring. By minimizing the deformation energy, nine 2×2 submatrices are obtained and can be added to the global stiffness matrix as shown in (39) and three 2×1 submatrices are obtained to be added to the global load vector as shown in (40):

$$\begin{aligned}
 p \begin{pmatrix} e_i \\ g_i \end{pmatrix} (e_i \ g_i) &\rightarrow \mathbf{K}_{ii}, \\
 p \begin{pmatrix} e_i \\ g_i \end{pmatrix} (e_j \ g_j) &\rightarrow \mathbf{K}_{ij}, \\
 p \begin{pmatrix} e_i \\ g_i \end{pmatrix} (e_k \ g_k) &\rightarrow \mathbf{K}_{ik}, \\
 p \begin{pmatrix} e_j \\ g_j \end{pmatrix} (e_i \ g_i) &\rightarrow \mathbf{K}_{ji}, \\
 p \begin{pmatrix} e_j \\ g_j \end{pmatrix} (e_j \ g_j) &\rightarrow \mathbf{K}_{jj}, \\
 p \begin{pmatrix} e_j \\ g_j \end{pmatrix} (e_k \ g_k) &\rightarrow \mathbf{K}_{jk}, \\
 p \begin{pmatrix} e_k \\ g_k \end{pmatrix} (e_i \ g_i) &\rightarrow \mathbf{K}_{ki}, \\
 p \begin{pmatrix} e_k \\ g_k \end{pmatrix} (e_j \ g_j) &\rightarrow \mathbf{K}_{kj}, \\
 p \begin{pmatrix} e_k \\ g_k \end{pmatrix} (e_k \ g_k) &\rightarrow \mathbf{K}_{kk}
 \end{aligned} \tag{39}$$

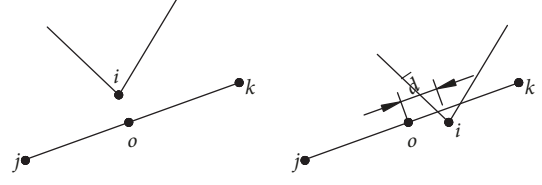


FIGURE 4: Tangential spring and its contribution to the global equation.

$$\begin{aligned}
 -\frac{pS_0}{l} \begin{pmatrix} e_i \\ g_i \end{pmatrix} &\rightarrow \mathbf{F}_i, \\
 -\frac{pS_0}{l} \begin{pmatrix} e_j \\ g_j \end{pmatrix} &\rightarrow \mathbf{F}_j, \\
 -\frac{pS_0}{l} \begin{pmatrix} e_k \\ g_k \end{pmatrix} &\rightarrow \mathbf{F}_k
 \end{aligned} \tag{40}$$

where \mathbf{F}_i is the generalized load vector acting on vertex i . This vector is a 2×1 vector. The stiffness matrix \mathbf{K}_{ii} is a 2×2 matrix related to vertex i , and $\mathbf{K}_{ij(i \neq j)}$ is a 2×2 matrix caused by contact restraints.

4.2. Tangential Stiffness Submatrix. As shown in Figure 4, the same contact pair is analyzed in the tangential direction. The point o is the lock point of vertex i at the entrance line jk . The coordinate and displacement of o are denoted as (x_o, y_o) and (u_o, v_o) . Similarly, by neglecting the second-order infinitesimal value, we generate the relative tangential distance \bar{d} along line jk :

$$\begin{aligned}
 \bar{d} &\approx \frac{(x_k - x_j \ y_k - y_j) \begin{pmatrix} x_i - x_o \\ y_i - y_o \end{pmatrix} + (x_k - x_j \ y_k - y_j) \begin{pmatrix} u_i - u_o \\ v_i - v_o \end{pmatrix}}{\sqrt{(x_j - x_k)^2 + (y_j - y_k)^2}} \\
 &= \frac{\bar{S}_0}{l} + \frac{1}{l} (x_k - x_j \ y_k - y_j) \begin{pmatrix} u_i \\ v_i \end{pmatrix} \\
 &\quad + \frac{1}{l} (x_j - x_k \ y_j - y_k) \begin{pmatrix} u_o \\ v_o \end{pmatrix}
 \end{aligned} \tag{41}$$

where

$$\bar{S}_0 = (x_k - x_j \ y_k - y_j) \begin{pmatrix} x_i - x_o \\ y_i - y_o \end{pmatrix} \tag{42}$$

and l is the same as in (35).

As mentioned in the second section, the displacement of point o can be obtained by a linear interpolation between (u_j, v_j) and (u_k, v_k) :

$$\begin{aligned}
 \begin{pmatrix} u_o \\ v_o \end{pmatrix} &= \frac{\sqrt{(x_o - x_k)^2 + (y_o - y_k)^2}}{l} \begin{pmatrix} u_j \\ v_j \end{pmatrix} \\
 &\quad + \frac{\sqrt{(x_o - x_j)^2 + (y_o - y_j)^2}}{l} \begin{pmatrix} u_k \\ v_k \end{pmatrix}
 \end{aligned} \tag{43}$$

Therefore, \bar{d} is illustrated as a formulation about (u_i, v_i) , (u_j, v_j) , and (u_k, v_k) :

$$\begin{aligned} \bar{d} = & \frac{\bar{S}_0}{l} + (\bar{e}_i \ \bar{g}_i) \begin{bmatrix} u_i \\ v_i \end{bmatrix} + (\bar{e}_j \ \bar{g}_j) \begin{bmatrix} u_j \\ v_j \end{bmatrix} \\ & + (\bar{e}_k \ \bar{g}_k) \begin{bmatrix} u_k \\ v_k \end{bmatrix} \end{aligned} \quad (44)$$

in which

$$\begin{aligned} \bar{e}_i &= \frac{x_k - x_j}{l}, \\ \bar{g}_i &= \frac{y_k - y_j}{l}, \\ \bar{e}_j &= \frac{x_j - x_k}{l^2} \sqrt{(x_0 - x_k)^2 + (y_0 - y_k)^2}, \\ \bar{g}_j &= \frac{y_j - y_k}{l^2} \sqrt{(x_0 - x_k)^2 + (y_0 - y_k)^2}, \\ \bar{e}_k &= \frac{x_j - x_k}{l^2} \sqrt{(x_0 - x_j)^2 + (y_0 - y_j)^2}, \\ \bar{g}_k &= \frac{y_j - y_k}{l^2} \sqrt{(x_0 - x_j)^2 + (y_0 - y_j)^2} \end{aligned} \quad (45)$$

When the contact pair is locked in the tangential direction according to Mohr-Coulomb friction law, the tangential spring is added and the related deformation energy is as follows:

$$\Pi_k = \frac{\bar{p}}{2} \bar{d}^2 \quad (46)$$

where \bar{p} is the stiffness of the tangential spring. By minimizing the deformation energy, nine 2×2 submatrices are obtained and can be added to the global stiffness matrix as shown in (47) and three 2×1 submatrices are obtained and can be added to the global load vector as shown in (48):

$$\begin{aligned} \bar{p} \begin{pmatrix} \bar{e}_i \\ \bar{g}_i \end{pmatrix} (\bar{e}_i \ \bar{g}_i) &\longrightarrow \mathbf{K}_{ii}, \\ \bar{p} \begin{pmatrix} \bar{e}_i \\ \bar{g}_i \end{pmatrix} (\bar{e}_j \ \bar{g}_j) &\longrightarrow \mathbf{K}_{ij}, \\ \bar{p} \begin{pmatrix} \bar{e}_i \\ \bar{g}_i \end{pmatrix} (\bar{e}_k \ \bar{g}_k) &\longrightarrow \mathbf{K}_{ik}, \\ \bar{p} \begin{pmatrix} \bar{e}_j \\ \bar{g}_j \end{pmatrix} (\bar{e}_i \ \bar{g}_i) &\longrightarrow \mathbf{K}_{ji}, \\ \bar{p} \begin{pmatrix} \bar{e}_j \\ \bar{g}_j \end{pmatrix} (\bar{e}_j \ \bar{g}_j) &\longrightarrow \mathbf{K}_{jj}, \\ \bar{p} \begin{pmatrix} \bar{e}_j \\ \bar{g}_j \end{pmatrix} (\bar{e}_k \ \bar{g}_k) &\longrightarrow \mathbf{K}_{jk} \end{aligned}$$

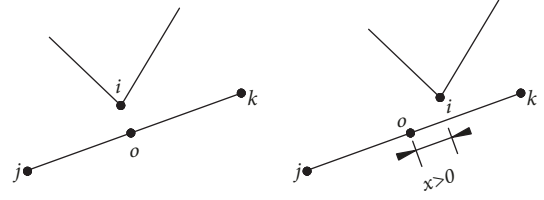


FIGURE 5: Friction force and its contribution to the global equation.

$$\begin{aligned} \bar{p} \begin{pmatrix} \bar{e}_k \\ \bar{g}_k \end{pmatrix} (\bar{e}_i \ \bar{g}_i) &\longrightarrow \mathbf{K}_{ki}, \\ \bar{p} \begin{pmatrix} \bar{e}_k \\ \bar{g}_k \end{pmatrix} (\bar{e}_j \ \bar{g}_j) &\longrightarrow \mathbf{K}_{kj}, \\ \bar{p} \begin{pmatrix} \bar{e}_k \\ \bar{g}_k \end{pmatrix} (\bar{e}_k \ \bar{g}_k) &\longrightarrow \mathbf{K}_{kk} \end{aligned} \quad (47)$$

$$\begin{aligned} -\frac{\bar{p}\bar{S}_0}{l} \begin{pmatrix} \bar{e}_i \\ \bar{g}_i \end{pmatrix} &\longrightarrow \mathbf{F}_i, \\ -\frac{\bar{p}\bar{S}_0}{l} \begin{pmatrix} \bar{e}_j \\ \bar{g}_j \end{pmatrix} &\longrightarrow \mathbf{F}_j, \\ -\frac{\bar{p}\bar{S}_0}{l} \begin{pmatrix} \bar{e}_k \\ \bar{g}_k \end{pmatrix} &\longrightarrow \mathbf{F}_k \end{aligned} \quad (48)$$

4.3. Friction Force Submatrix. As shown in Figure 5, the contact pair is reanalyzed in the tangential direction. When the vertex i slides along the entrance line jk , the tangential spring will be replaced by a pair of friction forces. The direction of friction is defined by the relative tangential displacement x between the master point i and its lock point o . Assuming that p is the normal spring stiffness and d is the normal interpenetration, the friction force should be

$$F = pds \tan(\varphi) \quad (49)$$

where φ is the friction angle and s is a sign function about x :

$$s = \text{sgn}(x) = \begin{cases} 1, & \text{if } x > 0 \\ 0, & \text{if } x = 0 \\ -1, & \text{if } x < 0 \end{cases} \quad (50)$$

Figure 5 provides a rule to determine whether x is positive. With this rule, the friction direction can be denoted as follows:

$$\begin{aligned} & \frac{((x_k - x_j) (y_k - y_j))}{\sqrt{(x_j - x_k)^2 + (y_j - y_k)^2}} \\ &= \frac{1}{l} ((x_k - x_j) (y_k - y_j)) \end{aligned} \quad (51)$$

When the value and direction of the friction force are ascertained, they can be treated as a pair of point loads acting at point i and point o . With the new displacement function, for one point located on the boundary, a point load will result in the load vector of two associated vertexes.

Finally, the contribution of friction force can be expressed as three 2×1 submatrices that can be added to the global load vector as shown in

$$\begin{aligned}
 & -F \begin{pmatrix} \frac{(x_k - x_j)}{l} \\ \frac{(y_k - y_j)}{l} \end{pmatrix} \rightarrow \mathbf{F}_i, \\
 & \frac{\sqrt{(x_0 - x_k)^2 + (y_0 - y_k)^2}}{l} F \begin{pmatrix} \frac{(x_k - x_j)}{l} \\ \frac{(y_k - y_j)}{l} \end{pmatrix} \rightarrow \mathbf{F}_j, \quad (52) \\
 & \frac{\sqrt{(x_0 - x_j)^2 + (y_0 - y_j)^2}}{l} F \begin{pmatrix} \frac{(x_k - x_j)}{l} \\ \frac{(y_k - y_j)}{l} \end{pmatrix} \rightarrow \mathbf{F}_k
 \end{aligned}$$

The global equations (13) are assembled by collecting the submatrices of all contacts between blocks and from (28) to (29) for all blocks, and they are further modified according to existing displacement boundary conditions. After solving the global equations, the states of each contact are inspected and the springs are adjusted to reflect the difference between the surmised contact states and the calculated contact states, which is called the “open-close” iteration. When the surmised contact state is consistent with the calculated contact state, the computation terminates and the freedom vectors are finally determined.

5. Numerical Examples

5.1. Sliding Problem. As shown in Figure 6, a rectangular block is laid on a ramp with a slope angle of 45° . The block and ramp have the same material properties: density $\rho=2.5 \times 10^3 \text{ kg/m}^3$, Young's modulus $E=35 \text{ MPa}$, Poisson's ratio $\nu=0.3$, and gravity acceleration $g=9.8 \text{ m/s}^2$. The external load is only generated via gravitational force. The three vertexes of the ramp are all fixed as the displacement boundary conditions.

Assuming the friction angle on the interface is φ , the block will slide along the ramp when $\varphi < 45^\circ$; in addition, its velocity has an analytical solution:

$$v = gt (\sin 45^\circ - \cos 45^\circ \tan \varphi) \quad (53)$$

where v is the sliding velocity (m/s) of the block and t is the elapsed time (s).

Four friction angle cases are studied: 0° , 15° , 30° , and 40° . Let the time step length $\Delta=0.02\text{s}$ and the max step displacement ratio $\delta=0.10$; subsequently, 35 time steps are calculated. Figure 7 shows a comparison between the analytical solutions and the results from the proposed scheme. The velocities from

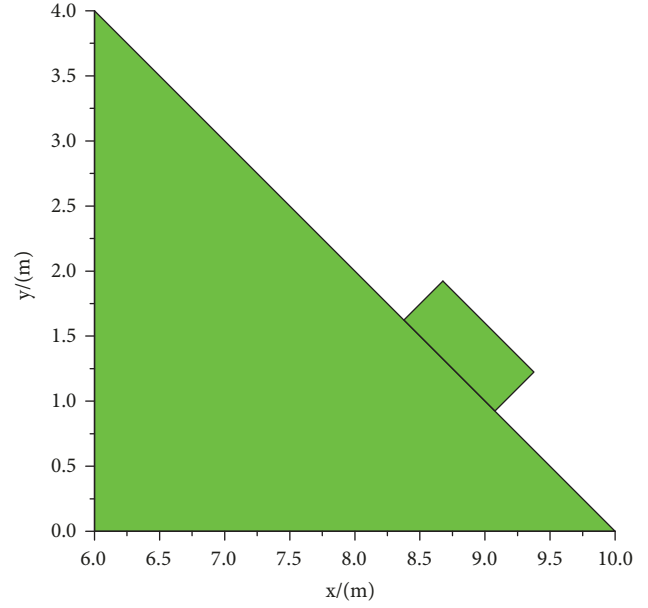


FIGURE 6: Block on the ramp with an inclined surface.

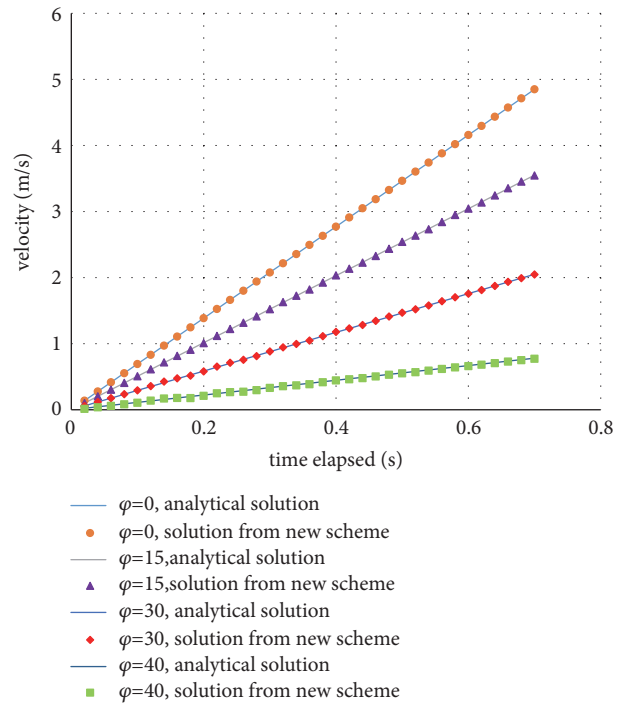


FIGURE 7: Comparison of the velocities between the analytical methods and proposed formulation.

the new scheme are consistent with the analytical solutions for all cases of friction angles.

The original DDA will provide high-precision results similar to this example, and the original DDA and the new formulation induce different stress distributions within the block. For this example, the stress results obtained by the original DDA and the proposed scheme are listed in Table 1. When the friction angle is 0° , the results of the

TABLE I: Comparison of the stress results from the proposed scheme and original DDA.

Friction Angle (°)	Original DDA				Proposed scheme				
	σ_x (N/mm ²)	σ_y (N/mm ²)	τ_{xy} (N/mm ²)	$\sigma_{x,max}$ (N/mm ²)	$\sigma_{x,min}$ (N/mm ²)	$\sigma_{y,max}$ (N/mm ²)	$\sigma_{y,min}$ (N/mm ²)	$\tau_{xy,max}$ (N/mm ²)	$\tau_{xy,min}$ (N/mm ²)
0	0.04167	0.04167	-0.39182	0.03929	0.03929	0.03929	0.03929	-0.39283	-0.39283
15	-0.75938	-3.24684	-1.76120	0.05732	-1.59622	-1.64227	-4.84594	-1.14239	-2.39011
30	-0.20619	-4.63249	-1.15462	0.91962	-1.34018	-0.58309	-8.68396	0.23368	-2.55740
40	-0.01983	-6.22811	-0.48968	1.41707	-1.45168	0.74530	-13.2077	1.77262	-2.76217

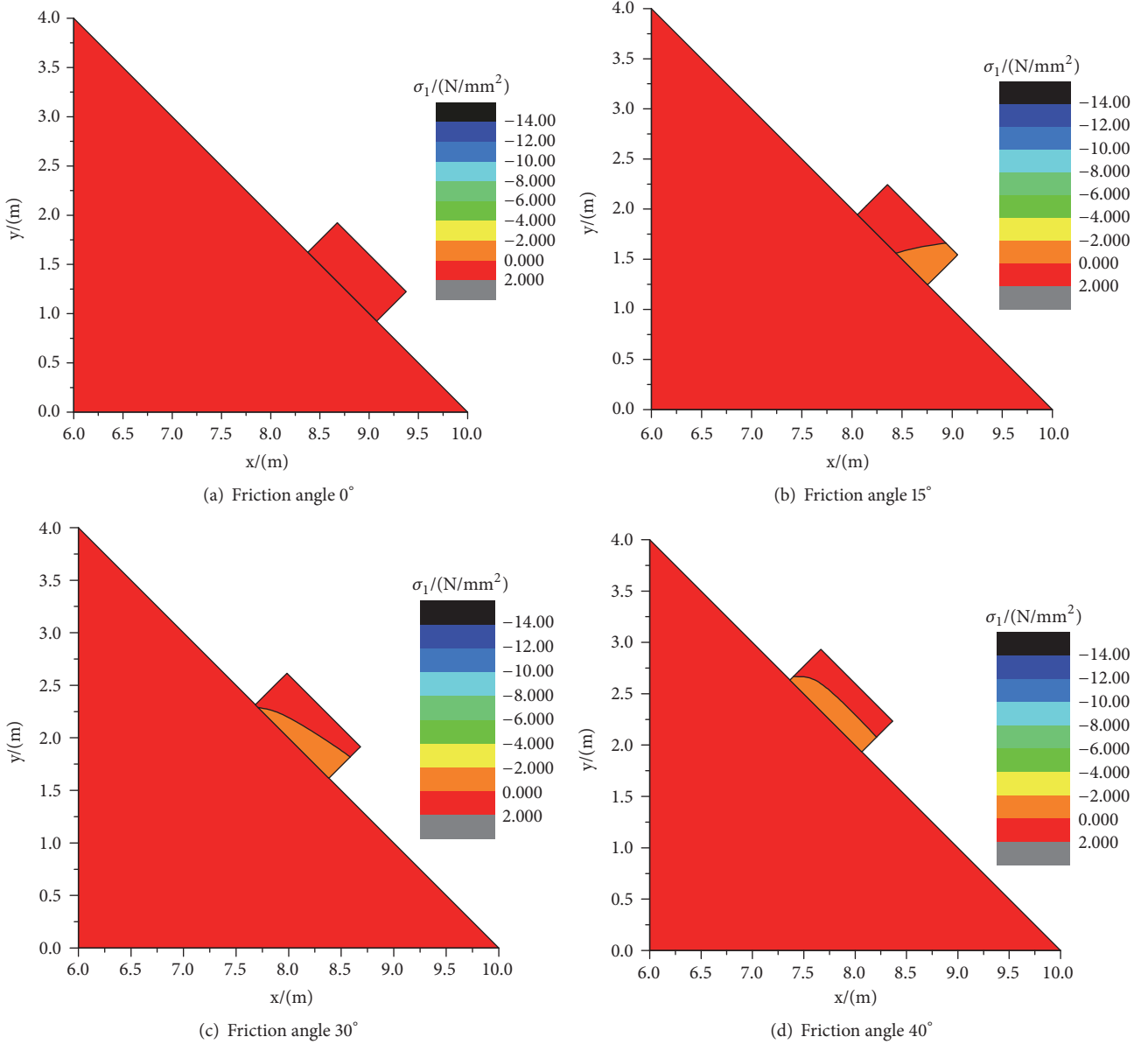


FIGURE 8: Distribution of the principal stress σ_1 with four different friction angles.

proposed scheme are basically consistent with the original DDA because in this case, the block has a constant stress distribution, which conforms to the assumption in the original DDA. However, the results of the proposed scheme are quite different from that of the original DDA in the case of friction

force. An analysis of the data indicates the stress results of the original DDA closely approximate the average value of the stress results provided by the proposed scheme.

Figures 8 and 9 show the principal stress distributions of the model with the four friction angles. In the case of friction

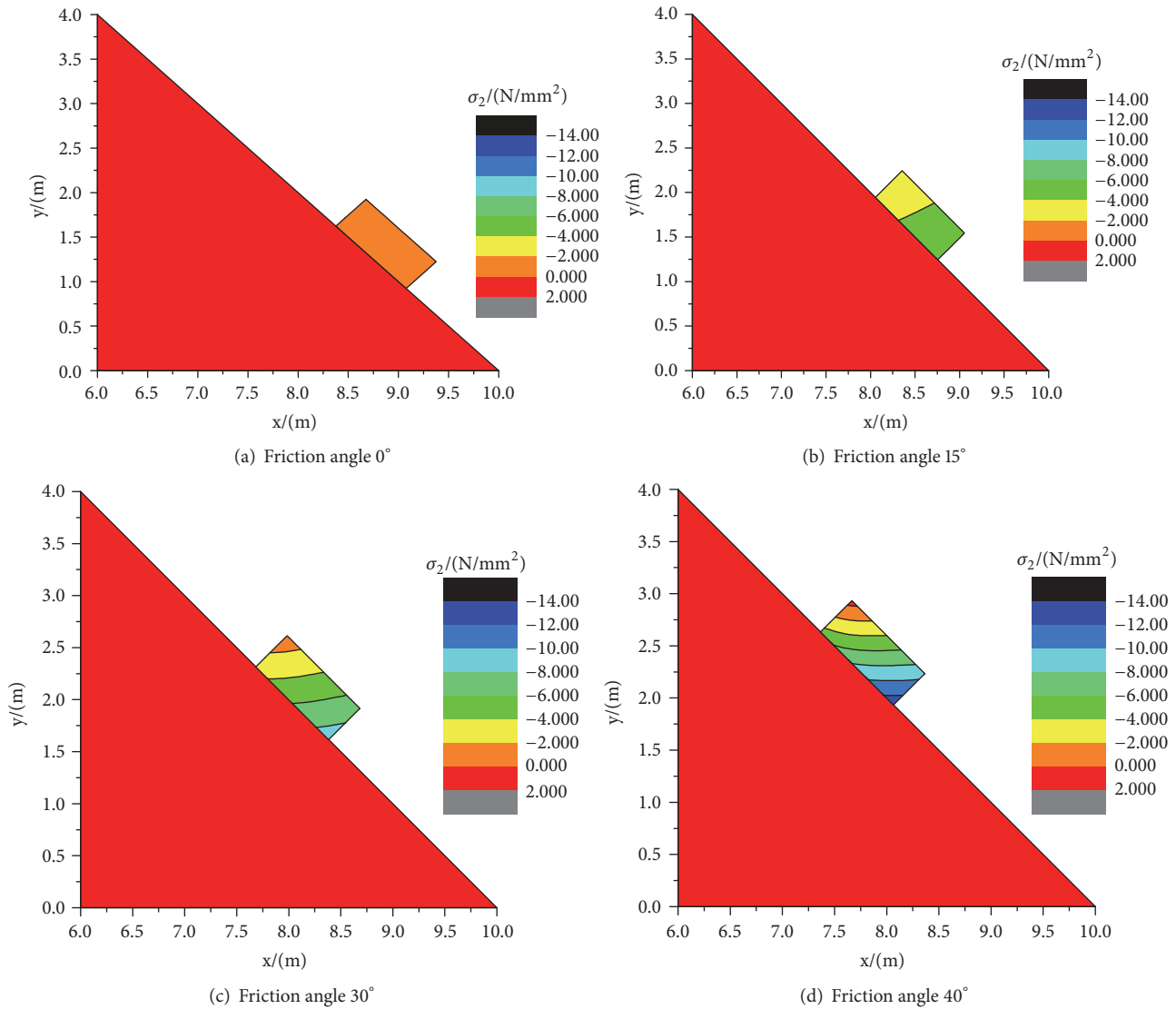


FIGURE 9: Distribution of the principal stress σ_2 with four different friction angles.

angle 0° , the principal stresses σ_1 and σ_2 are roughly constant in the block. Principal stress σ_1 is positive and σ_2 is negative, which indicate that the block is in tension along the direction of the principal stress σ_1 and compressed along the direction of σ_2 .

When the friction angle increases, the friction force acting along the bottom surface of the block gradually increases, which leads to apparent changes in the stress distributions. When friction force occurs, the minimum value of stress σ_1 is negative and remains at the bottom right corner, which means that this area is compressed. With increases in the friction angle, the minimum value of stress σ_1 decreases accordingly, and the compressive region spreads from the right to the left. When the friction angle is 40° , the regions close to the contact surface are almost compressed along the direction of principal stress σ_1 . The maximum value of stress σ_1 rises as the friction angle increases, which results in the distortion and deflection of the stress contour.

Principal stress σ_2 is negative throughout the block in most cases, which represents the compressive state within the entire block. The minimum value of principal stress σ_2 is located at the bottom right corner and falls rapidly as the friction angle increases. The maximum value of σ_2 occurs at the top left corner, and the value increases when the friction angle increases. When the friction angle reaches 40° , the maximum value of σ_2 is positive, which indicates that the top left corner is under tension.

5.2. Arch Bridge Problem. The arch bridge problem is a classical model designed by Shi and often used to test the validity of procedures based on the DDA. Figure 10 shows an arch bridge that consists of seven blocks. Each block has the same shape and area (0.17227 m^2), and four vertexes located at the leftmost and rightmost boundary are fixed as displacement boundary conditions. A vertical downward sustaining point load $P=0.05 \text{ kN}$ acts on the central block.

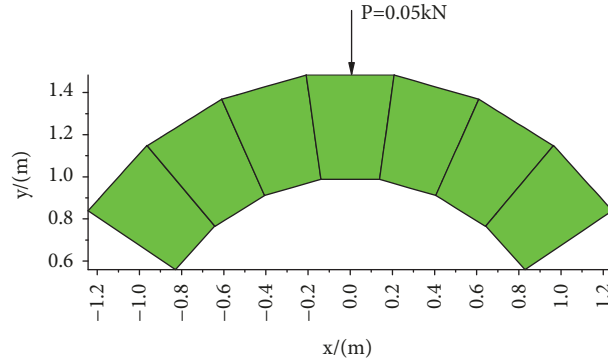


FIGURE 10: Arch bridge composed of seven identical blocks.

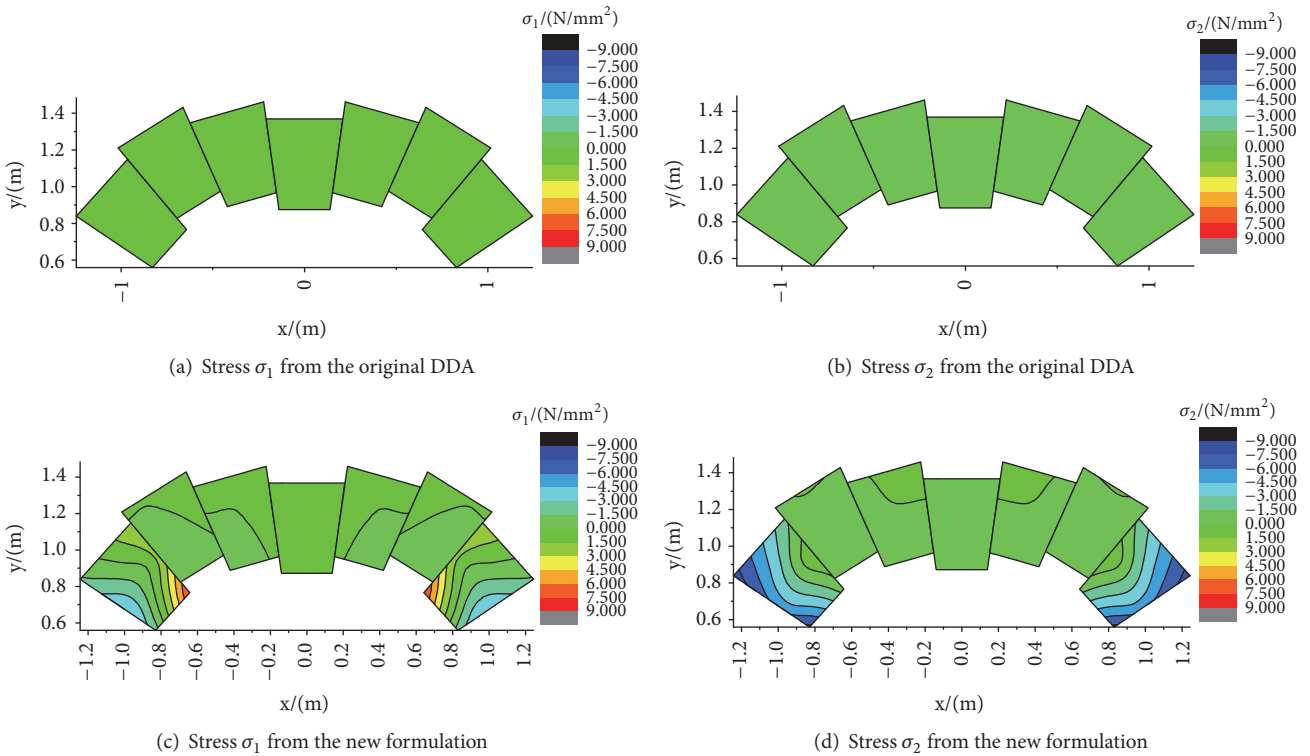


FIGURE 11: Stress distribution after 30 time steps in the case of no friction.

All blocks have the same property with the unit weight $\gamma=2.0 \text{ kN}/\text{m}^3$, Young's modulus $E=10 \text{ MPa}$, and Poisson's ratio $\nu=0.2$. Using the time step length $\Delta=0.01 \text{ s}$ and the max step displacement ratio $\delta=0.03$, we conduct a dynamic analysis of the example using the original DDA and the proposed formulation.

The configurations and stress distributions of the arch bridge for the original DDA and the new formulation after 30 time steps are shown in Figure 11, which assumes that no friction occurs between blocks. The results show that the new formulation generates a similar configuration as the original DDA. However, stress distributions from the new formulation are more explicit than those of the original DDA.

The stress distributions of the blocks fall into two categories. First, the stresses have significant variations in the

leftmost and rightmost blocks. The values of stress σ_1 and σ_2 are both negative in the regions close to fixed boundaries and change from negative to positive when the measured points move toward the center of the arch. For the boundary blocks, the regions close to fixed boundaries suffer biaxial compression, whereas the regions adjacent to the middle blocks are actually in tension. Second, the variations of all stresses are small in the middle blocks. An analysis of the stress distribution indicates that only the stress state of the central block is consistent with the original DDA. Along the direction of stress σ_1 , the bottom regions are in compression in the other middle blocks, whereas along the direction of stress σ_2 , some top regions are in tension. Finally, the results of the original DDA are still close to the average value of the new formulation.

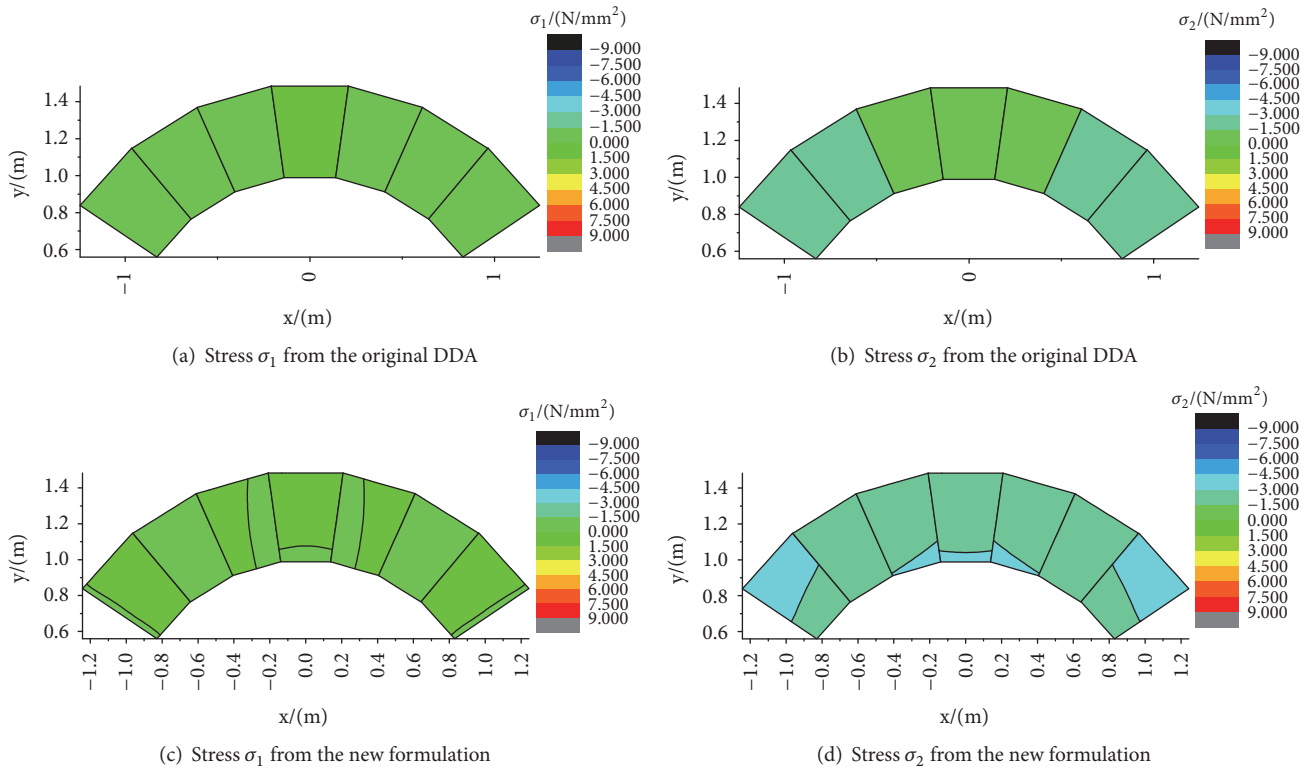


FIGURE 12: Stress distribution after 30 time steps in the case of a 30° friction angle.

Then, the above example is reanalyzed under the following assumptions: friction angle $\phi=30^\circ$ and cohesion $c=0$. The arch bridge is stable after 30 time steps, and the vertical load acting on the central block is distributed to the adjacent blocks one by one. The configurations and stress distributions from the original DDA and the new formulation are illustrated in Figure 12.

The two methods both obtain a negative stress σ_2 throughout the model, and its absolute value is larger than stress σ_1 , which indicates extrusion between blocks. Compared with the original DDA, the new formulation reveals additional details about the extrusion effect. In the middle blocks, stress σ_2 reaches its minimum value at the bottom; however, stress σ_2 reaches its minimum value at the top in the leftmost and rightmost blocks. Thus, the extrusion effect varies with the position of a block in this arch model. Combined with stress σ_1 , most of the blocks are not in biaxial compression everywhere. For a boundary block, stress σ_1 changes from negative to positive when the measurement point moves toward the center. For the central block, stress σ_1 changes from positive to negative when the measurement point moves downward. An analysis of the joint surfaces shows that stress σ_1 always has a different sign on both sides.

The difference between the two methods is not remarkable in Figure 12, which is caused by the stress tag setting. For ease of comparison, all panels in Figures 11 and 12 adopt the same stress tag; however, the stress distribution obtained by the new formulation is more complicated. Figure 13 shows the stress distribution with an independent tag.

5.3. Voronoi Polygons Problem. Voronoi polygonal structures are commonly used to simulate the microstructures of crystals and other materials, and they present considerable advantages for creating complex particle shapes and sizes. Generally, the particles are typical polygons, and for each particle, the number of edges may be different. The new formulation is preferable for simulating block models generated by the Voronoi map method.

As shown in Figure 14, the block model with a Voronoi polygonal structure is laid on a ramp. The ramp and blocks have the same properties, with a unit weight $\gamma=21 \text{ kN/m}^3$, Young's modulus $E=10 \text{ GPa}$, and Poisson's ratio $\nu=0.25$. The mechanical parameters of the joints throughout the model have a friction angle of $\phi=40^\circ$ and cohesion of $c=1 \text{ MPa}$. The contact surface between the blocks and the ramp uses the same parameters applied to the joints. Four vertices of the ramp are fixed as displacement boundary conditions.

Assuming that the external load is only generated via gravitational force, we conduct a static analysis of the example with the original DDA and the new formulation, and it includes a time step length of $\Delta=0.01 \text{ s}$ and a max step displacement ratio of $\delta=0.03$. The configurations and stress distributions after 55 time steps are illustrated in Figure 15.

The two methods obtain a negative stress σ_2 throughout the model, and the absolute value increases when the measurement point moves downward because only gravity guides the stress distribution and deformation. Compared with stress σ_2 , stress σ_1 has small absolute values and variations in the model. Except for some regions close to joints, the results

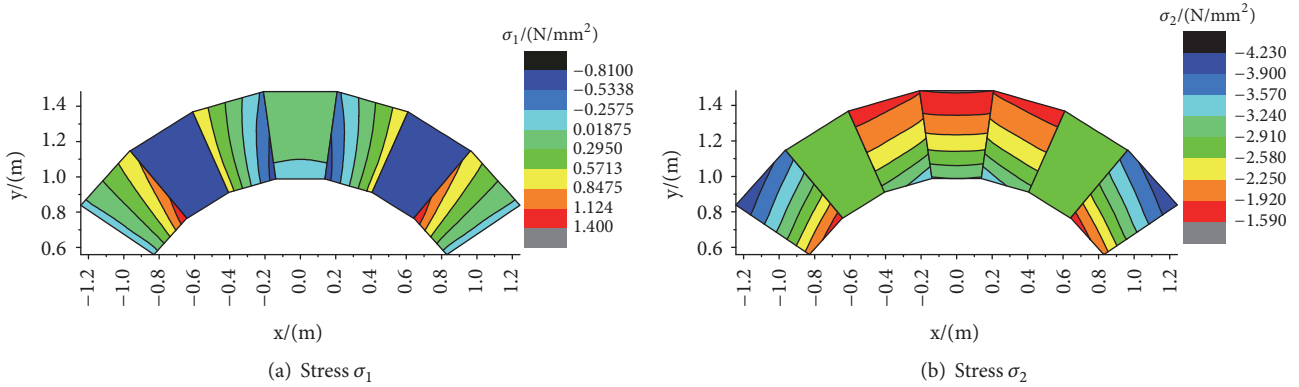


FIGURE 13: Detailed stress distribution from the new formulation in the case of a 30° friction angle.

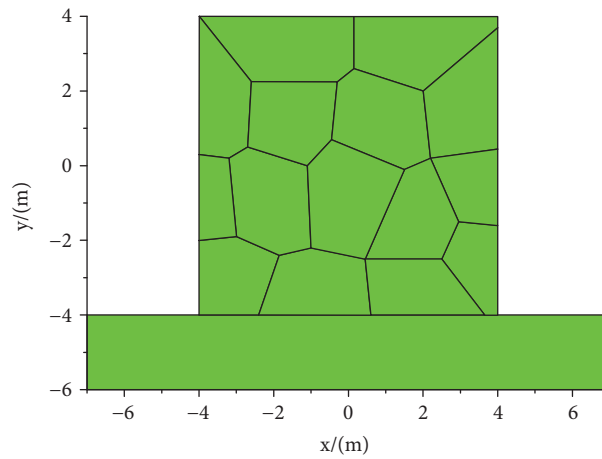


FIGURE 14: Block model with a Voronoi polygonal structure.

from the new formulation reveal that stress σ_1 ranges from -18.54 N/mm^2 to 18.04 N/mm^2 .

Compared with the original DDA, the new formulation shows issues with the stress concentration around some vertices. In the original DDA, the contact forces are developed by mutual movements between blocks regardless of whether a static or dynamic analysis is performed. This approach is not changed in the proposed formulation, which results in concentrated forces acting on vertices. Therefore, the stress concentration issue is reasonable.

A horizontal rightward sustaining point load $P=200 \text{ kN}$ is added to act on the upper left block in Figure 16. The example is reanalyzed with the same calculation parameters and time steps as before.

Figure 17 shows the configurations and stress distributions from the original DDA and the new formulation. The distributions of stress σ_1 and stress σ_2 have clearly changed, especially for the new formulation. Most regions are in biaxial compression under a combination of a horizontal pushing force and gravitational force. The upper left block presents the maximum pressure stress σ_1 . Because of the effect of the horizontal pushing force, the regions with a positive stress σ_1 increased and the area decreased. Stress σ_1 increases around

some joints because of the transmission of the horizontal pushing force.

6. Discussion

The new formulation improves upon existing approaches because the complicated and continuous stress distributions within block elements are provided and all edges of blocks remain straight. Regardless of whether artificial joints or finite element meshes are involved in the block, the block dissection should be executed and the stresses will be discontinuous within the block. The new formulation avoids block dissection and generates a continuous stress distribution. When higher-order displacement functions are adopted in the DDA, the edges of blocks are always transformed from lines to curves, which induce problems for contact detection. To satisfy the contact constraints between blocks, the edges should be dissected and then contact detection should be carefully performed. In the new formulation, the edges of blocks remain straight lines, which means that contact detection can be processed according to the original DDA. Of course, the DDA with higher-order displacement functions presents certain remarkable abilities; e.g., one straight

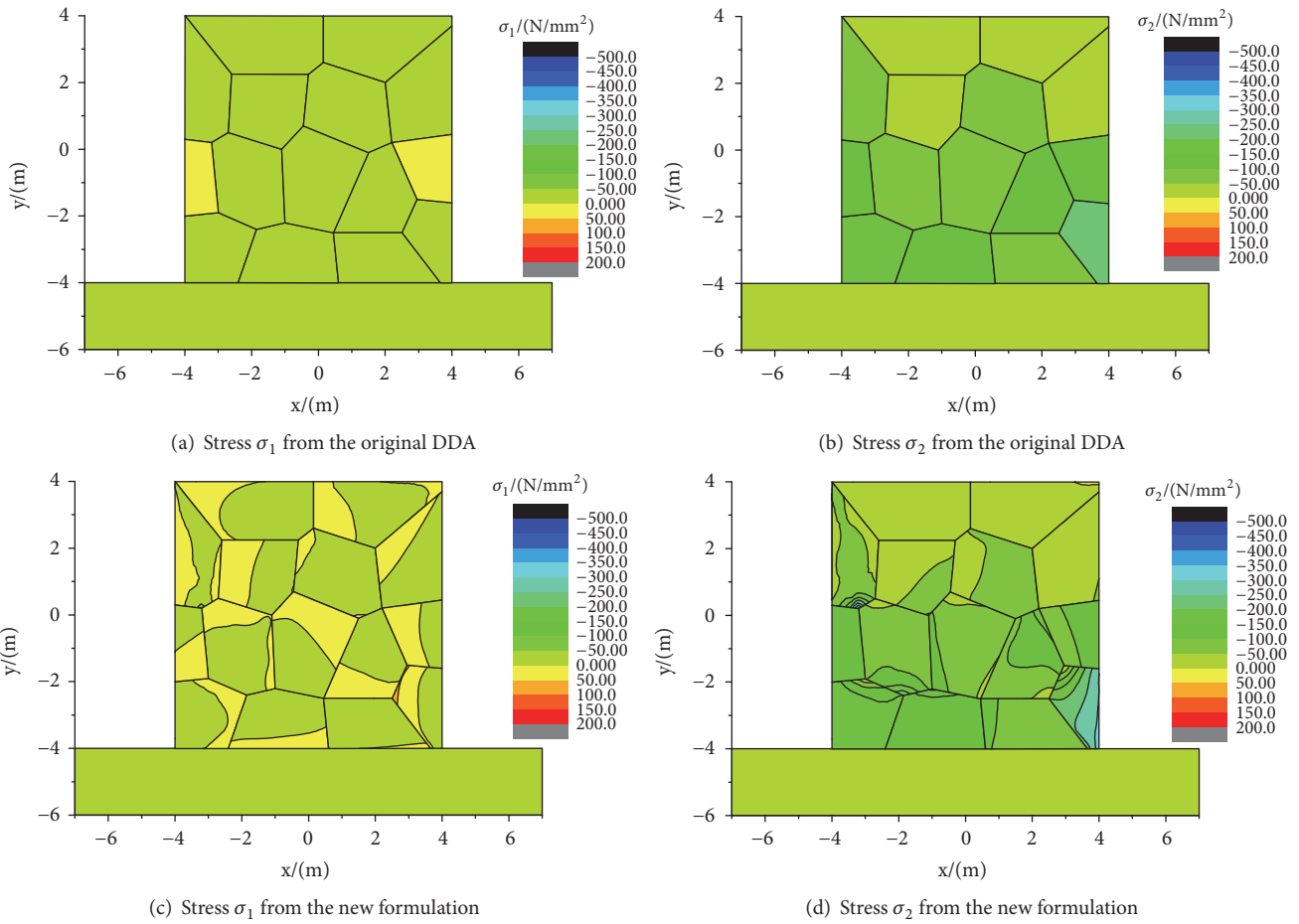


FIGURE 15: Stress distribution after 55 time steps under gravitational force.

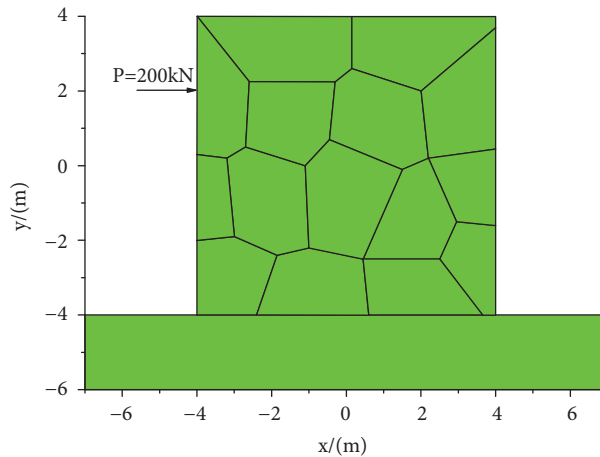


FIGURE 16: Block model sustaining a horizontal rightward load.

line polygon can be transformed into one curved polygon. However, for most rocks, the strain in the block is small, even if the block is on the point of rupture. Accordingly, the deformation of a block is small compared with the movement, and the assumption that the edges of a block are still straight is acceptable.

The limitation of the new formulation is that only those blocks with the shape of a convex polygon can be included in the block system because the displacement function based on the Wachspress interpolation is not suitable for concave polygons [33]. The displacements of block vertices form new freedom vectors in the proposed formulation, which implies

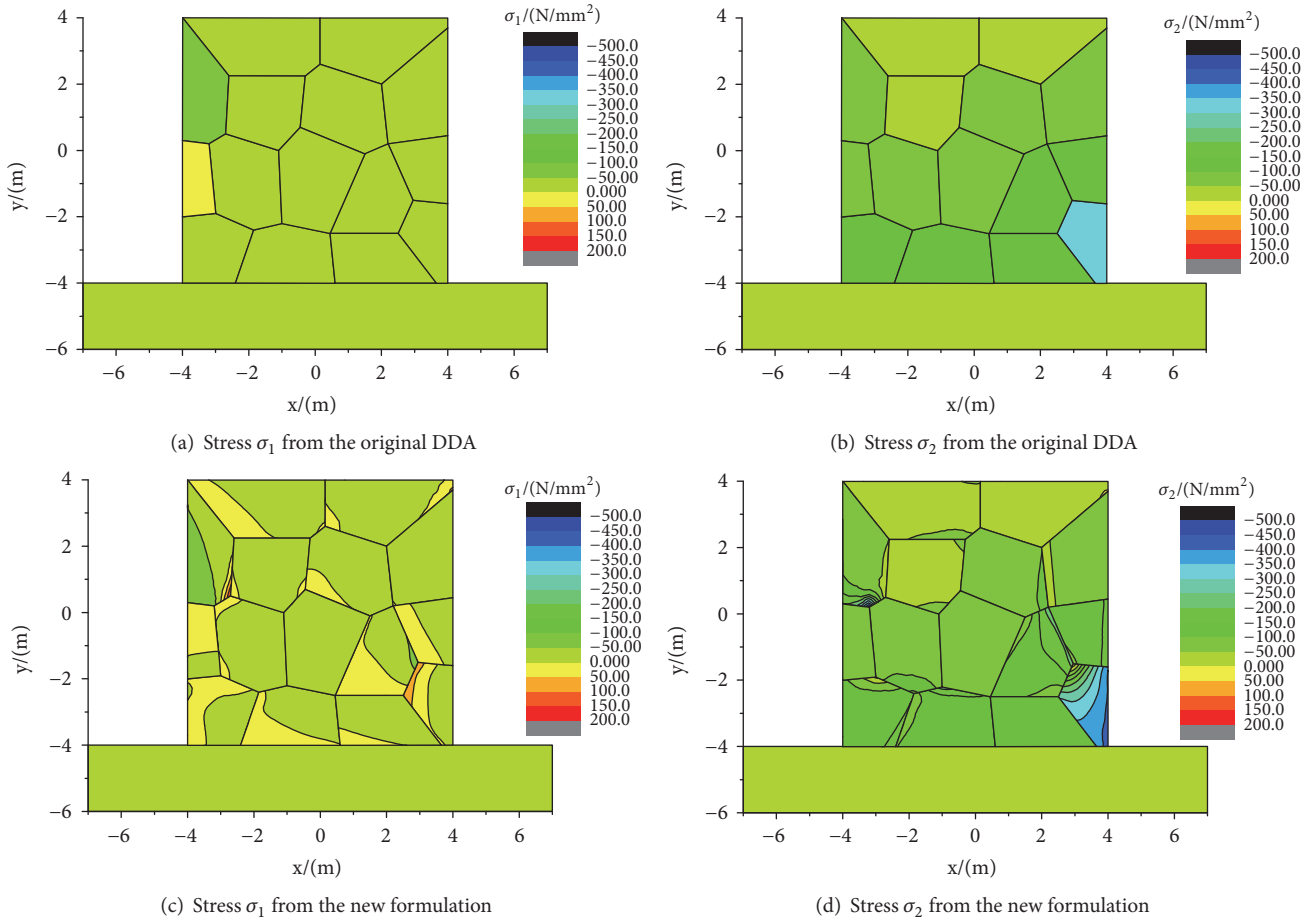


FIGURE 17: Stress distribution after 55 time steps under the new load conditions.

that, for one block, the detailed level of stress distribution relies on the number of its vertexes rather than the number of Hammer points involved in the integration. The extreme case is a block with three vertexes, for which only constant stresses can be gained by the proposed formulation. Because the Wachspress interpolation scheme is effective for all non-concave polygons, the issue can be solved by appending extra vertexes on edges. However, introducing additional vertexes to generate a detailed stress distribution is not feasible in the new formulation because the $m+1$ th time step is always calculated based on the configuration results at the end of the m th time step. If one additional vertex is added on one edge, then the original nonconcave polygon may be transformed to a polygon containing a concave angle after deformation and the computation will fail. A more robust displacement interpolation scheme is expected to be developed for the uniform processing of various polygons, which will remedy the limitations of the proposed formulation.

7. Conclusions

To acquire a more detailed stress distribution, the displacement function of block in DDA is modified in this paper. For each block, the displacements of its vertexes constitute new freedom vectors, the displacement is expressed based

on Wachspress interpolation function, and formulations of stiffness and force matrices are then derived accordingly. The contacts between blocks are still governed as in the original DDA; thus, contact detection can be processed based on the original DDA because the edges of blocks are always straight. Three examples are analyzed using the original DDA and the proposed formulation. The results show that the new scheme has similar configurations as the original DDA but generates more detailed and continuous stress distributions within block elements. The new formulation has greater advantages because it provides complicated and continuous stress distributions while avoiding extra work in the contact analysis. Because of the limitations of existing Wachspress interpolation approaches, the new formulation is not suitable for concave polygons and lacks the ability to obtain detailed stress distributions of blocks with limited vertexes. An advanced displacement interpolation scheme suitable for uniformly processing various polygons is expected, and it will improve the robustness of the new formulation.

Data Availability

The data used to support the findings of this study are available from the corresponding author upon request.

Conflicts of Interest

The authors declare that they have no conflicts of interest.

Acknowledgments

This study is supported by the Open Research Programme of the Hubei Key Laboratory of Disaster Prevention and Mitigation (under Grant no. 2017KJZ03) and National Natural Science Funds (Project no. 51409150).

References

- [1] GH. Shi, "Discontinuous Deformation Analysis A New Numerical Model for the Statics and," Tech. Rep., Dynamics of Block Systems. Department of Civil Engineering University of California, Berkeley.
- [2] J.-H. Wu and C.-H. Chen, "Application of DDA to simulate characteristics of the tsaoiling landslide," *Computers & Geosciences*, vol. 38, no. 5, pp. 741–750, 2011.
- [3] Y. H. Hatzor, A. A. Arzi, Y. Zaslavsky, and A. Shapira, "Dynamic stability analysis of jointed rock slopes using the DDA method: king Herod's Palace, Masada, Israel," *International Journal of Rock Mechanics & Mining Sciences*, vol. 41, no. 5, pp. 813–832, 2004.
- [4] G. Chen, L. Zheng, Y. Zhang, and J. Wu, "Numerical simulation in rockfall analysis: A close comparison of 2-D and 3-D DDA," *Rock Mechanics and Rock Engineering*, vol. 46, no. 3, pp. 527–541, 2013.
- [5] Y. Ning, J. Yang, G. Ma, and P. Chen, "Modelling rock blasting considering explosion gas penetration using discontinuous deformation analysis," *Rock Mechanics & Rock Engineering*, vol. 44, no. 4, pp. 483–490, 2011.
- [6] H. Zhu, W. Wu, J. Chen, G. Ma, X. Liu, and X. Zhuang, "Integration of three dimensional discontinuous deformation analysis (DDA) with binocular photogrammetry for stability analysis of tunnels in blocky rockmass," *Tunnelling and Underground Space Technology*, vol. 51, pp. 30–40, 2016.
- [7] G. Zhang, Z. Lei, and H. Cheng, "Shear creep simulation of structural plane of rock mass based on discontinuous deformation analysis," *Mathematical Problems in Engineering*, vol. 2017, Article ID 1582825, 2017.
- [8] L. Q. Choo, Z. Zhao, H. Chen, and Q. Tian, "Hydraulic fracturing modeling using the discontinuous deformation analysis (DDA) method," *Computers & Geosciences*, vol. 76, pp. 12–22, 2016.
- [9] C. Tang, S. Tang, B. Gong, and H. Bai, "Discontinuous deformation and displacement analysis: From continuous to discontinuous," *Science China Technological Sciences*, vol. 58, no. 9, pp. 1567–1574, 2015.
- [10] X. Fu, Q. Sheng, Y. Zhang, and J. Chen, "Application of the discontinuous deformation analysis method to stress wave propagation through a one-dimensional rock mass," *International Journal of Rock Mechanics and Mining Sciences*, vol. 80, pp. 155–170, 2015.
- [11] MM. MacLaughlin and N. Sitar, "Rigid body rotations in DDA," in *Proceedings of the in. Proceedings of the first international forum on Discontinuous Deformation Analysis (DDA) and simulations of discontinuous media*, pp. 620–35, 1996.
- [12] C. Y. Koo and J. C. Chern, "Modification of the DDA method for rigid block Problems," *International Journal of Rock Mechanics and Mining Sciences*, vol. 35, no. 6, pp. 683–693, 1998.
- [13] Y. M. Cheng and Y. H. Zhang, "Rigid body rotation and block internal discretization in DDA analysis," *International Journal for Numerical and Analytical Methods in Geomechanics*, vol. 24, no. 6, pp. 567–578, 2000.
- [14] W. Jiang and H. Zheng, "An efficient remedy for the false volume expansion of DDA when simulating large rotation," *Computers & Geosciences*, vol. 70, pp. 18–23, 2015.
- [15] Y. Cai, G. Liang, and GH. Shi, *Studying impact problem by LDDA method. Discontinuous Deformation analysis (DDA) and simulations of discontinuous media*, TSI Press, Discontinuous Deformation analysis (DDA) and simulations of discontinuous media, 1996.
- [16] H. Zheng and W. Jiang, "Discontinuous deformation analysis based on complementary theory," *Science China Technological Sciences*, vol. 52, no. 9, pp. 2547–2554, 2009.
- [17] W. Jiang and H. Zheng, "Discontinuous deformation analysis based on variational inequality theory," *International Journal of Computational Methods*, vol. 8, no. 2, pp. 193–208, 2011.
- [18] H. Zheng, P. Zhang, and X. Du, "Dual form of discontinuous deformation analysis," *Computer Methods Applied Mechanics and Engineering*, vol. 305, pp. 196–216, 2016.
- [19] S. Amir Reza Beyabanaki and A. C. Bagtzoglou, "Non-rigid disk-based DDA with a new contact model," *Computers & Geosciences*, vol. 49, pp. 25–35, 2013.
- [20] Q. Jiang, Y. Chen, C. Zhou, and M.-C. R. Yeung, "Kinetic energy dissipation and convergence criterion of discontinuous deformations analysis (DDA) for geotechnical engineering," *Rock Mechanics and Rock Engineering*, vol. 46, no. 6, pp. 1443–1460, 2013.
- [21] G. Shi, "Producing joint polygons, cutting joint blocks and finding key blocks for general free surfaces," *Chinese Journal of Rock Mechanics and Engineering*, vol. 25, no. 11, pp. 2161–2170, 2006.
- [22] J. Wang, G. Lin, and J. Liu, "Static and dynamic stability analysis using 3D-DDA with incision body scheme," *Earthquake Engineering and Engineering Vibration*, vol. 5, no. 2, pp. 273–283, 2006.
- [23] J. Liu, Q. D. Geng, and X. J. Kong, "A fast common plane identification algorithm for 3D contact problem," *Computers & Geosciences*, vol. 36, no. 1-2, pp. 41–51, 2009.
- [24] A. R. Keneti, A. Jafari, and J.-H. Wu, "A new algorithm to identify contact patterns between convex blocks for three-dimensional discontinuous deformation analysis," *Computers & Geosciences*, vol. 35, no. 5, pp. 746–759, 2008.
- [25] G. H. Shi, "Contact theory," *Science China Technological Sciences*, vol. 58, no. 9, pp. 1450–1496, 2015.
- [26] TC. Ke, TSI Press, *Discontinuous Deformation analysis (DDA) and simulations of discontinuous media*, 1996.
- [27] C. T. Lin, B. Amadei, J. Jung, and J. Dwyer, "Extensions of discontinuous deformation analysis for jointed rock masses," *International Journal of Rock Mechanics and Mining Sciences & Geomechanics Abstracts*, vol. 33, no. 7, pp. 671–694, 1996.
- [28] JC. Chern, CY. Koo, and S. Chen, "Development of second-order displacement function for DDA and Manifold method. Working Forum on the Manifold Method of Material Analysis," *Chen S. Development of second-order displacement function for DDA and Manifold method. Working Forum on the Manifold Method of Material Analysis*, pp. 183–202, 1995.
- [29] S. A. R. Beyabanaki, A. Jafari, and M. R. Yeung, "High-order three-dimensional discontinuous deformation analysis (3-D DDA)," *International Journal for Numerical Methods in Biomedical Engineering*, vol. 26, no. 12, pp. 1522–1547, 2010.

- [30] KK. Shyu, *Nodal-based discontinuous deformation analysis [Ph.D. thesis]*, Department of Civil Engineering, University of California, Berkeley, 1993.
- [31] CS. Chang, *Nonlinear dynamic discontinues deformation analysis with finite element meshed block system [Ph.D. thesis]*, Department of Civil Engineering, University of California, Berkeley, 1994.
- [32] Y. Ma, H. Zheng, and C. Li, "Research on discontinuous deformation analysis coupled with meshfree methods," *Yanshilixue Yu Gongcheng Xuebao/Chinese Journal of Rock Mechanics and Engineering*, vol. 26, no. 2, pp. 4195–4201, 2007.
- [33] N. Sukumar and E. A. Malsch, "Recent advances in the construction of polygonal finite element interpolants," *Archives of Computational Methods in Engineering: State-of-the-Art Reviews*, vol. 13, no. 1, pp. 129–163, 2006.
- [34] G. Manzini, A. Russo, and N. Sukumar, "New perspectives on polygonal and polyhedral finite element methods," *Mathematical Models and Methods in Applied Sciences*, vol. 24, no. 8, pp. 1665–1699, 2014.
- [35] G. Dasgupta, "Interpolants within convex polygons: wachpress' shape functions," *Journal of Aerospace Engineering*, vol. 16, no. 1, pp. 1–8, 2003.
- [36] V. V. Belikov and A. Y. Semenov, "Non-Sibsonian interpolation on arbitrary system of points in Euclidean space and adaptive isolines generation," *Applied Numerical Mathematics*, vol. 32, no. 4, pp. 371–387, 2000.
- [37] R. Sibson, "A vector identity for the Dirichlet tessellation," *Mathematical Proceedings of the Cambridge Philosophical Society*, vol. 87, no. 1, pp. 151–155, 1980.
- [38] N. Sukumar, "Construction of polygonal interpolants: a maximum entropy approach," *International Journal for Numerical Methods in Engineering*, vol. 61, no. 12, pp. 2159–2181, 2004.
- [39] E. Cueto, N. Sukumar, B. Calvo, M. A. Martínez, J. Cegoñino, and M. Doblaré, "Overview and Recent Advances in Natural Neighbour Galerkin Methods," *Archives of Computational Methods in Engineering: State-of-the-Art Reviews*, vol. 10, no. 4, 2003.
- [40] E. T. Jaynes, "On The Rationale of Maximum-Entropy Methods," *Proceedings of the IEEE*, vol. 70, no. 9, pp. 939–952, 1982.

